Development of a novel segmented mesh MicroMegas detector for neutron beam profiling

M. Diakaki[a,b,*], E. Berthoumieux[a], T. Papaevangelou[a], F. Gunsing[a], G. Tsiledakis[a], E. Dupont[a], S. Anvar[a], L. Audouin[c], F. Aznar[f,g], F. Belloni[a,d], E. Ferrer-Ribas[a], T. Dafni[f], D. Desforge[a], T. Geralis[e], Y. Giomataris[a], J. Heyse[d], F. J. Iguaz[f,a], D. Jourde[a], M. Kebbiri[a], C. Paradela[d], P. Sizun[a], P. Schillebeeckx[d], L. Tassan-Got[c], E. Virique[a]

[a] *CEA Irfu, Université Paris-Saclay, F-91191 Gif-sur-Yvette, France*
[b] *European Organization for Nuclear Research (CERN), Switzerland*
[c] *Institut de Physique Nucléaire, CNRS-IN2P3, Univ. Paris-Sud, Université Paris-Saclay, F-91406 Orsay Cedex, France*
[d] *European Commission, Joint Research Centre, Geel, Retieseweg 111, B-2440 Geel, Belgium*
[e] *NCSR Demokritos, GR-15341 Ag. Paraskevi, Athens, Greece*
[f] *Grupo de Física Nuclear y Astropartículas, Universidad de Zaragoza, Pedro Cerbuna 12, 50009 Zaragoza, Spain*
[g] *Centro Universitario de la Defensa, Universidad de Zaragoza, Ctra. de Huesca s/n, 50090, Zaragoza, Spain*

Abstract

A novel MicroMegas detector based on microbulk technology with an embedded XY strip structure was developed, obtained by segmenting both the mesh and the anode in perpendicular directions. This results in a very low-mass device with good energy and spatial resolution capabilities. Such a detector is practically "transparent" to neutrons, being ideal for in-beam neutron measurements and can be used as a quasi-online neutron beam profiler at neutron time-of-flight facilities. A dedicated front end electronics and acquisition system has been developed and used. The first studies of this new detection system are presented and discussed.

Keywords: microbulk MicroMegas, Position-sensitive detector, neutron beam profile

---

*Present address: CEA DEN, Cadarache, F-13108 Saint Paul lez Durance, France
Email address: Maria.DIAKAKI@cea.fr (M. Diakaki)

June 7, 2018

1. Introduction

The MicroMegas detector is a two stage gaseous detector [1], widely used in nuclear and high energy physics thanks to the high versatility in the detection of different kinds of radiation, from X-rays to fission fragments. The gas-filled region of the detector is separated into two volumes, by the so-called "*micromesh*" (or simply "*mesh*"): the *drift region* between cathode and mesh and the *amplification region* between mesh and anode. Electrons, produced in the drift region by ionisation of gas molecules from the incoming radiation, are drifted by the low electric field applied in this region (typically 0.1 kV/cm) towards the micromesh and pass through the holes to the amplification region. Due to the high field applied in this region, they are amplified in electron avalanches. The "*microbulk*" MicroMegas is nowadays a well established production technology for the structure of the amplification region of the detector [2], based on the etching of a double sided copper-clad polyimide (Kapton) foil. Typically, the copper and Kapton layers are 5 µm and 50 µm thick, respectively. The micromesh is etched from the top copper layer and thus forms a thin electrode with holes of 40 to 50 µm, distributed in different topologies. Thanks to the uniformity of the amplification region of the microbulk Micromegas, leading to a high homogeneity of the electric field between the micromesh and the anode, microbulk detectors offer nowadays one of the best energy resolutions achievable for gaseous detectors operating in proportional mode [3]. Additional advantages are the very low material budget, the high radiopurity of the material [4] and the long term stability [5]. These features make these detectors suitable for a variety of applications, such as rare event searches [6] or neutron detection [7].

In order to form a position sensitive microbulk, the bottom copper layer (anode) is usually segmented into strips or pixels, connected to the readout electronics through conductive vias and strip lines in extra layers, added below the anode. Thus, if two-dimensional particle hit information is required, two extra conductive planes (copper) and two Kapton layers need to be added. This manufacturing process is complicated and time-consuming and involves a considerable risk of damaging the detector. Furthermore, the addition of extra material for the readout strips makes the detector less attractive for applications where a minimal material budget is mandatory, such as in-beam neutron measurements. Finally, the charge produced in the amplification volume is shared among the anode pads. In standard XY detectors, the pads are interconnected to form strip readouts, so an unequal charge sharing between the two strip layers can occur.

Recently, a novel microbulk detector prototype has been presented, with the micromesh segmented for the first time [8]. The anode is also segmented into perpendicular strips. The goal of this new design was to simplify the construction process of a microbulk detector with a real two-dimensional readout structure (better determination of the two coordinates of the position from the charge in the amplification area) and to minimise the material budget of the detector. The design was optimised by testing a series of small size prototypes in order to maintain the good microbulk properties (presented in [8]). Based on the topology of the prototype with the best performances the first real size detector has been produced at the CERN EP-DT-EF workshop [1]. The characteristics and performance of this new detection system are presented here.

2. Detector setup

The main challenges to overcome with this kind of detector are the microbulk design, the need of auto-trigger electronics in the absence of an undivided mesh electrode as well as the high voltage distribution to the mesh strips in order to ensure the proper field in the amplification volume. All these challenges had to be overcome as described in this section.

[1] The Engineering Facilities (EF) section of the Detector Technologies (DT) group of the Experimental Physics (EP) Department of CERN.

2.1. Segmented mesh microbulk

A schematic view of the amplification structure of the segmented mesh microbulk is shown in Fig. 1.

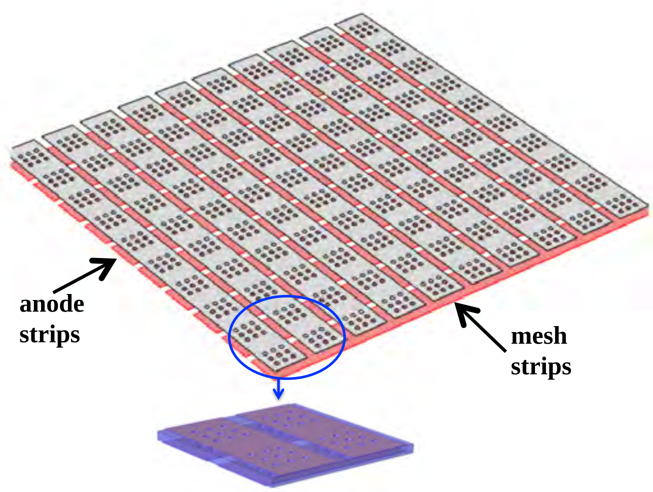

Figure 1: (Color online) Schematic view of the segmented mesh microbulk detector. The holes of the micromesh are arranged in matrices with a fixed number of holes/column in the overlapping region of mesh and anode strips.

The manufacturing process, described in detail in ref. [8], starts with a double sided copper-clad 50 µm thick Kapton foil as raw material. In the first step, the mesh holes are photolithographically created, respecting the special topology shown in Fig. 1. In a second step, the strips in perpendicular directions are formed on both sides of the copper-clad Kapton foil. The study of the prototypes revealed that the main challenge in the manufacturing process, although it is much simpler than for the previous microbulks with two-dimensional strip readout, lies upon the proper etching of the Kapton below the mesh holes, without completely removing the material between the mesh strips, and the good alignment of the anode strip edges with the regions without holes of the mesh strips. Furthermore, it has been shown (by simulations of the electric field lines and by measurements with the prototypes) that the hole topology on the mesh strips as well as the interstrip gaps considerably influence the performance of the detector. Ideally, the mesh holes need to be homogeneously distributed on the strip surface and the interstrip gaps reduced as much as possible in order to minimise the loss of electrons and the consequent deterioration of the good energy resolution of the microbulk.

The first two detectors were made, based on the 2×2 cm^2 prototype which showed the best performance, with an active area of 6×6 cm^2 divided into 60+60 strips with 1 mm width. The characteristics of the microbulks can be found in Table 1.

	Interstrip gap (µm)	**Hole topology**
Prototype	35	10 columns - 8 holes/column
Detector No. 1	35	5 columns - 8 holes/column
		5 columns - 7 holes/column
Detector No. 2	60	9 columns - 8 holes/column

Table 1: Segmented mesh microbulk characteristics. The holes had a diameter of 60 µm and a pitch of 100 µm for all three detectors. In detectors No. 1 and 2 the interstrip spacing and hole topology have been modified.

The microbulk structures of Detector No. 1 and 2 were manufactured on a 4 mm thick PCB ring in order to ensure the detector rigidity and allow the connection to the front-end electronics. A photo of the sensitive area of the final detector is shown in Fig. 2. The drift gap typically used for the measurements reported here was 1 cm.

2.2. Electronics system

Unlike in non-segmented Micromegas detectors, where the micromesh signal can be used to trigger the readout electronics connected to the anode strips,

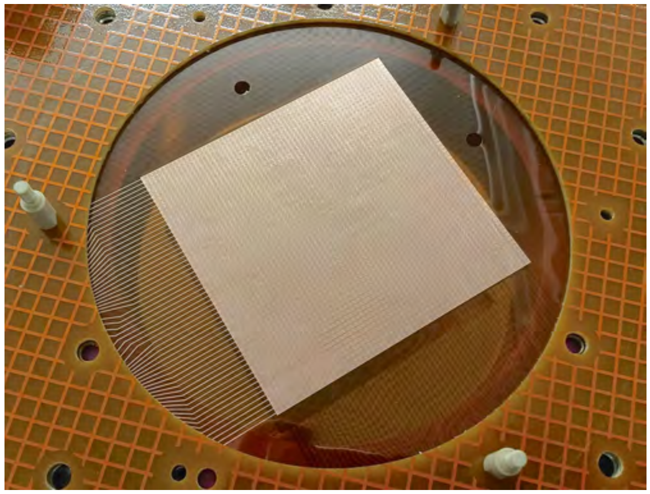

Figure 2: (Color online) Photo of the first 6×6 cm^2 segmented mesh microbulk detector produced, mounted on the thick PCB.

the readout electronics used for a segmented mesh microbulk needs to be self-triggering. For this purpose the GET electronics was chosen (R-CoBo configuration, see below) based on the AGET ASIC chip [9, 10]. This chip is adapted to Time Projection Chamber readouts, allowing to reconstruct the event track in the detector gas. It features 64 analog channels, each equipped with a Charge Sensitive Preamplifier (CSA) with adjustable input sensitivity (maximum dynamic range 120 fC - 10 pC) and peaking time (70 ns - 1 µs) values, and the possibility to work with both positive and negative input signal polarities. The CSA output signal is stored in an analogue memory based on a Switched Capacitor Array (SCA) of 512 samples with adjustable sampling frequency (1 - 100 MHz). An external 12-bit ADC is used for the readout at 25 MHz frequency. Three readout modes (all channels / only channels that passed the chosen threshold value / selected channels) and adjustable number of memory cells (1 - 512) are available. The GET electronics provides a threshold and multiplicity trigger when running in the auto-trigger mode, as well as the possibility to accept an external trigger. In the version of the GET electronics used for this work, 4 AGET chips and a four channel ADC were soldered on the

AsAd (ASIC Support & Analog-Digital conversion) card, and a concentration board (“reduced” CoBo or R-CoBo) was used as a communication intermediary between the AsAd and the computer.

Special front-end (FE) cards were designed and built, to properly connect the mesh and anode strips to the AsAd board for the strip readout, provide the high voltage to the mesh strips and protect the AGET chips from potential discharges in the detector. These functionalities were divided in two cards, one directly plugged on the detector PCB (different design for the mesh and anode strips) and one directly plugged on the AsAd card with the protection diodes against the discharges. Series of tests were performed with X-rays and with a neutron beam at the 10 m flight path neutron beam line of the GELINA facility of JRC-Geel [11], which helped to finalise the design.

3. Detector characterisation

3.1. Characterisation with low energy X-rays

The detector performance was tested with X-rays, using a ^{55}Fe source (E_{K_α}=5.9 keV, E_{K_β}=6.5 keV). The detector chamber was filled with a gas mixture of 95% argon - 5% isobutane (iC_4H_{10}) at atmospheric pressure, circulated at a constant flow of ∼6 Nl/h. The detector voltages were typically V_{mesh} = 340 V and V_{drift} = 430 V. The whole AGET + front-end electronics chain was used to record the X-ray signals. For each X-ray energy deposition in the detector gas, mesh and anode strips were read out. Typical signals recorded from the electronics for one X-ray energy deposition, with 100 MHz sampling frequency, are shown in Fig. 3. A good signal-to-noise ratio was achieved and typically 1-3 consecutive strips for the mesh and the anode were triggering an event for this gas, voltage and threshold settings.

The electron transparency as a function of the ratio of the electric fields in the drift and amplification region is shown in Fig. 4. The detector presents a wide plateau in the transparency for $E_{\mathrm{d}}/E_{\mathrm{m}} \geq 0.001$, where E_{d} and E_{m} are the electric field in the drift and the amplification region respectively.

Reading each strip of the mesh and the anode electrodes independently allows for an efficient rejection of background events. Criteria can be applied for the selection of good events, either independent of or dependent on the type of radiation to be measured. First, signals induced on mesh and anode strips are simultaneous and have equal but inverted amplitude by construction. Slight differences in the recorded signal amplitudes can occur due to different electronics channel gains. Indeed, for all the tests with this detector with different particles and types of gas the mean ratio of the charge induced on the anode to the one induced on the mesh was close to 1 with a moderate variation of ± 0.1 (similar to the one of Fig. 10). Furthermore, criteria such as the consecutivity of the strips hit and the maximum multiplicity expected can be applied to various types of radiation. More specifically, for X-ray energy deposition, the simultaneity of the strip signals can also be considered as a criterion for the good events. The above mentioned criteria were applied and only less than 1% of the total events were rejected in the case of the optimised setup, thanks to the very low noise. The total amplitude distributions, obtained by adding the signal amplitudes from anode and mesh strips separately for each event, were clean and the argon escape peak at 2.9 keV was clearly separated. Optimum energy resolution was observed with the source irradiating only the central 20 to 30 strips of the detector. An exemplary total amplitude distribution for anode signals is shown in Fig. 5.

The energy resolution was estimated by fitting the dominant ^{55}Fe peak with two gaussians corresponding to the expected K_α and K_β peaks and was (13.0 $\pm$ 0.5)% (FWHM). This energy resolution is comparable to, or even better than microbulk detectors with non-segmented micromeshes [2, 12]. The energy resolution observed for the mesh strips was slightly worse, (13.5$\pm$ 0.5)%, possibly due to additional noise related to the circuit for the application of high voltage at these strips. The theoretical energy resolution for proportional counters at a given energy E is given by $\mathrm{FWHM}_E/E = 2.35 \times \sqrt{W(F+b)/E}$, where W is the energy required to form an ion pair, F the Fano factor and b the gain fluctuations factor due to the avalanches [13]. Thus, the corresponding theoretical limit of the energy resolution for a non-segmented 50 µm microbulk at this energy is ∼11% [14]. The experimental resolution obtained with the new segmented microbulk detector was slightly worse. This can be attributed to various factors related to the microbulk structure as well as the electronics and the electrical connections.

Firstly, the loss of ionisation electrons in the interstrip gaps and areas on the mesh strips without holes (see Fig. 1) deteriorates the resolution. The value stated above was observed for the detector No. 1 (Table 1), while the energy resolution of detector No. 2 was of the order of 16-17%, attributed to the larger interstrip gap and the reduced number of micromesh holes, resulting in increased electron losses. Furthermore, the best resolution reported in ref. [8] for the small segmented microbulk prototypes was 11.5% FWHM at 5.9 keV with the same gas mixture and different electronics, and it was shown that misalignments in the mesh and anode strips can significantly deteriorate the resolution.

Secondly, the amplitude variations among the strips (due to electronics gain variations, different charge collection etc.) affect the resolution. In order to check the amplitude variations among the strip signals, the whole detector surface was irradiated with X-rays from an uncollimated ^{55}Fe source and the position of the dominant peak in the amplitude spectrum was determined for each strip. This most probable amplitude is shown in Fig. 6 as a function of the strip number. The amplitude varies very little among the central 40 strips, within 2% (1σ), while it drops rapidly for the 10 strips at the borders, due to drift field inhomogeneities. Because of these field inhomogeneities at the border, the energy resolution was degraded and reached values of 16-17%. This is a known issue for such detectors and can be solved with the addition of an extra thin electrode surrounding the active area ("rim" electrode) [15].

Another factor deteriorating the resolution in the case of the segmented microbulk is the incomplete charge collection from strip signals not passing the acquisition threshold chosen. Indeed, the best resolution values were achieved when this threshold was kept as low as possible.

Finally, some grounding issues on the detector PCB were discovered (the bottom and top grounding layers were not properly interconnected), creating extra noise to the system, which were bypassed with external connections.

The above mentioned results indicate that with the optimisation of the hole topology and interstrip gap and with good alignment of the strips, as well as special attention to the grounding design during the microbulk and PCB fabrication processes respectively, this already good energy resolution value could be further improved.

A radiography of a copper mask using 5.9 keV X-rays is shown in Fig. 7. A very clean image of the copper mask was obtained, indicating good event reconstruction capabilities of the new system.

3.2. Characterisation of operation as neutron beam profiler

The new detection system was tested with respect to the detection of neutrons at the Orphée reactor of the laboratory LLB (Laboratoire Léon Brillouin) of CEA-Saclay [16, 17]. It is a 14 MW reactor with a small core highly enriched in ^{235}U, which provides a high neutron density, surrounded by a heavy water reflector tank to obtain a high thermal flux (3×10^{14} n/cm^{2}s). The detector was placed at the G3-2 neutron beam line in order to study the performance in the detection of the neutrons and the reconstruction of neutron beam profiles. At this station, the neutron flux has a nearly Maxwellian distribution peaking at a wavelength of 1.7 Å (corresponding to a neutron kinetic energy of 3 meV). B_4C and Cd masks with different shapes were used for localised neutron irradiation of the detector. In most cases, extra PMMA plates were used in order to reduce the very high counting rate that was causing dead time in the readout electronics.

The detection of neutrons is performed by the interaction of neutrons with a target (neutron converter) that undergoes a nuclear reaction with a well known cross section. Thus, the detection of neutrons turns into the detection of the reaction products from the neutron interaction. The neutron converter used was ^{6}Li, producing a triton and a ^{4}He particle via the well known ^{6}Li(n,t)^{4}He reaction [18]. Provided that the incoming neutron energy is negligible compared to the reaction Q-value the two reaction products are emitted back to back with energies E_{t}=2.73 MeV and $E_{^4\mathrm{He}}$=2.05 MeV. A 9 cm diameter ^{6}LiF layer of 91.8 µg/cm^2 was deposited on a thin aluminised mylar backing (used as the drift electrode). The detection gas used in this case was 90% argon - 10 %CO_2 at atmospheric pressure and the drift region was 1 cm thick. When the charged particles from the neutron interactions exit the target and travel through the detection gas, electrons are produced along their track in the drift region and are detected by consecutive anode and mesh strips of the MicroMegas detector. The first strip that gives a signal corresponds to the point of the particle track that is closest to the mesh while the last one corresponds to the point of interaction of the neutron with the neutron converter and is used for the reconstruction of the beam profile (the principle is shown in Fig. 8). The sampling frequency for the recording of the signals was 100 MHz.

The characteristics of the different masks used are listed in Table 2. The detector was mounted on an X-Y table in order to irradiate different points of the ^{6}LiF layer and estimate the homogeneity and the reconstruction of the same image at different positions of the detector. In order to estimate the homogeneity of the converter at the surface covered by the detector, the rectangular hole was used to sample a surface of approximately 6×6 cm^2, and the counting rate of the alpha particle peak at the various points was compared. In total 71 points were sampled, with a step of 5-8 mm. The converter was found to be homogeneous within less than 5% (1 σ). At the edges of the detector the alpha counting rate was generally smaller, up to 10-12%.

Mask shape	**Dimensions (mm)**
Circular hole	⌀ 5
Circular hole	⌀ 2
Square hole	5 × 5
Rectangular hole	1 × 5

Table 2: Characteristics of the masks used. In most cases, PMMA plates were used in order to reduce the neutron fluence (by a factor of 16).

3.2.1. Charged particle tracks selection

As shown in Fig. 9, the multiplicities typically varied from 1-9 strips. The small multiplicities mainly correspond to forward tracks (i.e. perpendicular to the sample surface) or tracks nearly parallel to one strip (1-2 strips), and the higher multiplicities correspond to tracks emitted at bigger angles with respect to the normal to the sample, crossing many strips. The distinct shape of the distribution is probably due to tracks that are not crossing the strips perpendicularly, promoting specific regions of the low multiplicities in the case of alpha particles and of the high multiplicities in the case of tritons.

The first event selection criterion was, also in this case, the balance of the induced charge at the mesh and anode strips. In Fig. 10, a typical distribution of the ratio between the total amplitudes of anode and mesh signals for all events in a run is shown. The ratio is centered at 0.98 (and not 1, due to different electronics channel gains between the mesh and anode strips), with tails that are attributed to events with incomplete charge collection either on the mesh or anode strips (due to single strip threshold effects, i.e. a signal not recorded from a strip because the amplitude is smaller than the threshold applied). The events with ratio smaller than 0.8 and bigger than 1.2 were rejected.

The next two criteria are based on the nearly continuous ionisation of the charged particle in the gas, taking advantage of the independent recording of the strip signals. Firstly, the strips recorded in an event had to be consecutive, both for the mesh and the anode. Secondly, the time difference Δt between the first and the last strip that gave a signal (Fig. 8) should be less than or equal to the expected drift time of the electrons from the converter to the mesh electrode, i.e. $\Delta t \leq d/v$, where d is the drift distance and v is the velocity of the electrons in the drift region which depends on the gas and the electric field applied. Taking into account that the time 0 corresponds to the time of the first strip that gave a signal (auto-triggering mode), the maximum Δt value corresponds to tracks that reach the mesh electrode, as the one schematically shown in Fig. 8. The value of Δt is smaller for tracks with bigger angles with respect to the normal of the target surface and goes down to 0 for tracks nearly parallel to the target surface. A typical histogram of the experimental Δt values obtained for tracks recorded by the mesh and the anode strips can be found in Fig. 10. Indeed, assuming d =1 cm and v = 3.4 cm/s for this type of gas and electric field strength applied in the drift region [19], it occurs that $\Delta t \leq$ (294 $\pm$ 30) ns, which agrees with the observation (Fig. 10).

Typical total amplitude distributions for mesh and anode strips can be found in Fig. 11. Single strip threshold effects were observed, mainly for the very low amplitude signals. This is more evident for the anode strips because of extra noise that was observed during the measurement, necessitating a higher single strip acquisition threshold. Nevertheless, with the criteria applied, the background or not well recorded charged particle events were sufficiently rejected and the final total amplitude distribution histograms were clean.

3.2.2. Monte Carlo simulations

In order to estimate the expected energy deposition of the alphas and the tritons in the gas and understand the experimental total amplitude histograms, Monte Carlo simulations were performed with the codes FLUKA [20, 21] and GEANT4 [22, 23]. The geometry of the detector setup was implemented in detail, and thermal neutron beams of different cross section shapes corresponding to the masks used were impinging on different points of the ^{6}LiF target. The energy deposition of the alphas and the tritons was scored independently in the active gas volume of the detector. Results obtained for the 5 mm diameter circular mask can be found in Fig. 12.

As expected, alpha particles have a shorter range than the tritons due to their larger energy loss per unit path length. Thus, alpha particles emitted in forward directions have on average lost less energy in the ^{6}LiF layer and have longer tracks than those emitted under larger angles (Fig. 12a). As a result, the energy deposition of the alpha tracks is recorded by a few strips around the point of interaction of the neutron beam with the ^{6}LiF layer ($\pm$ 1 cm) and corresponds to the right peak of the total amplitude distribution

(Fig. 12b). On the contrary, the tritons deposit little energy along their track and thus have longer tracks that extend to the edges of the detector (Fig. 12a). Consequently, they deposit only part of their total energy in the gas and form the lower peaks/bumps of the experimental total amplitude histograms (Fig. 12b). Furthermore, they are recorded with small signals by each strip, and thus the experimental total amplitude distribution from these tracks is more sensitive to single strip threshold effects and gain variations (mainly at the edges of the detector). This difference of the alpha/triton tracks observed from the simulations is reflected in the experimental amplitudes of signals for the different strips, as shown in Fig. 13.

Taking the above into account, it can be concluded that the qualitative agreement between the simulated energy deposition histogram (Fig. 12b) and the experimental total amplitude histograms (Fig. 11), even in the absence of the proper resolution function, is quite satisfactory, especially in the case of the mesh strips. Moreover, the criteria applied are also excluding some of the triton tracks, for the reasons explained above.

Based on the simulated energy deposition of the alpha/triton peaks, the calibration of the experimental spectra was made, and the single strip threshold applied at the acquisition was estimated to be 65±6 keV (for the mesh strips).

Finally, the neutron detection efficiency of the new system with this ^{6}LiF layer was estimated to be as low as 0.21%, according to the simulations. The results obtained with GEANT4 were in perfect agreement with the FLUKA results.

3.2.3. Image reconstruction with neutron beam

An example of the neutron beam profile obtained when using the latest strip as measure for the neutron interaction point in the converter can be seen in Fig. 14, for the 5mm diameter circular mask. A clear improvement in the neutron beam profile reconstruction was observed when the good events selected with the above mentioned criteria were used (Fig 14 (right)).

The spatial resolution of the detector, assuming that the interaction can take place anywhere on the 1.1 mm wide strip, is expected to be (1.1 mm)/$\sqrt{12} \approx$ 0.32 mm (the width of the strip was 1.065 mm according to the technical drawings). In order to experimentally confirm the spatial resolution, the circular beam profiles obtained were fitted with a function corresponding to a gaussian convoluted with a step function. The 2D formula of this function is given in Eq. 1, also used in ref. [24].

$$B(x,y) = \frac{A}{2\alpha}(\mathrm{Erf}(\alpha + \sqrt{f(x,y)}) - \mathrm{Erf}(\sqrt{f(x,y)} - \alpha)) \tag{1}$$

where

$\mathrm{Erf}(u) = \frac{2}{\sqrt{\pi}} \int_0^u e^{-t^2} \mathrm{d}t$ and

$f(x,y) = \frac{1}{2(1-\rho)^2}(\frac{(x-\mu_x)^2}{\sigma_x^2} + \frac{(y-\mu_y)^2}{\sigma_y^2} - 2\rho\frac{(x-\mu_x)(y-\mu_y)}{\sigma_x\sigma_y})$

containing 7 free parameters: A is a normalisation factor, α is the parameter of the step function which determines the "plateau" at the center of the beam profile, ρ is the correlation coefficient between the two axes and $\sigma_x(1-\rho)$ and $\sigma_y(1-\rho)$ the standard deviations in the frame of the principal axes of the gaussian. The σ values reflect the spatial resolution of the beam profile convoluted with the neutron beam broadening due to the scattering at the edges of the masks. However, the latter value is difficult to estimate due to the inhomogeneities of the mask edges.

An exemplary fit using Eq. 1 can be found in Fig. 15, for the profile of the circular mask of 5 mm diameter. The 1D projections of the slices corresponding to the middle Y (anode)- and X (mesh)- strips onto the X- and Y- axis respectively are also shown in Fig. 15. The ρ parameter was found to be close to zero, while $\sigma_x \approx \sigma_y$ for the circular profiles and were in the range 0.45-0.55 mm (depending on the profile, with fitting parameter uncertainties of the order of 1-2%), including the non negligible neutron beam broadening (mainly due to the neutron scattering at the edges of the masks and the PMMA plates).

The reconstructed images shown in Fig. 14 and Fig. 15 are obtained by assuming that the neutron interaction position is defined by the latest strip, without any deeper localisation on the 1.1 mm wide strip. In an effort to further improve the image reconstruction, a correction factor was implemented for the position of the point of interaction, with the simplified assumption that the energy loss is constant for the two last strips that had a signal, i.e. the first two strips at the track of the emitted particle from the point of interaction. With this assumption, if $\mathrm{d}E1$ and $\mathrm{d}E2$ are the charges deposited at the last strip and the previous one respectively, and $\mathrm{d}X1$ and $\mathrm{d}X2$ the track length projections onto the respective strips, then $\mathrm{d}X1 = \mathrm{d}X2 \times \frac{\mathrm{d}E1}{\mathrm{d}E2}$, with $\mathrm{d}X2 = 1$ strip, since the previous strip is fully crossed. From this relation the position of the neutron interaction $\mathrm{d}X1$ on the last strip was determined. The value of the correction factor $\frac{\mathrm{d}E1}{\mathrm{d}E2}$ is expected to follow a uniform distribution between 0 and 1. Due to the amplitude threshold effects, it deviated from the expected uniform distribution at borders. To take this effect into account, in a first approximation, when this value was close to 0 or 1, it was re-sampled with a random distribution, in order to achieve an approximately uniform distribution.

With the above described procedure, a finer binning could be used for the reconstruction of the beam profiles, since the probability of interaction was no longer equally probable on the 1.1 mm wide strip, and the quality of the images was further improved. The beam profiles obtained can be found in Fig. 16.

The quality of the images is improved with the more refined analysis. By fitting such profiles with Eq. 1 or the projection of the middle X- and Y- slices of the 2D profile onto the Y- and the X-axis respectively with the 1D expression of this formula, the σ_x and σ_y values were reduced to 0.32 ± 0.05 mm. (the uncertainty corresponds to the standard deviation of the σ values from all the profiles fitted).

A final remark on the detector spatial resolution capabilities is worth to be added. The collimator with the rectangular hole (see Table 2) was used in order to irradiate different points on the ^{6}LiF foil within ± 1 mm (i.e. the strip size). By taking into account the mean values of the reconstructed images, it was possible to resolve shifts of the point of irradiation with good accuracy. More precisely, the agreement between the expected shifts (X-Y table) and the reconstructed ones was better than 1% for shifts bigger than 0.2 mm. These results, although they cannot be directly used as spatial resolution results, indicate the high resolving power of the system developed.

In order to further improve the spatial resolution capabilities of this new detector and fully exploit it as a Time Projection Chamber, a more detailed methodology is needed, with simulations taking into account the energy loss per strip, the gain variations among the strips and the response function of the electronics, and it will be part of the future development of the system.

4. Conclusions

A new microbulk MicroMegas detector has been developed, having for the first time both the mesh and the anode segmented into strips at perpendicular directions, offering a real 2D readout scheme, with the minimum material budget possible with such detectors. The 6×6 cm^2 detector has been successfully tested with X-rays and neutron beams, showing very good energy and spatial resolution and offering the possibility to reconstruct charged particle trajectories in the active gas region. Possible improvements have been pointed out from this work and considered for the next detector and electronics designs, such as the improvement of the microbulk fabrication precision (using Laser Direct Imaging for example) leading to the reduction of the micromesh regions without holes and the reproducibility of the fabrication process, a better grounding scheme, the addition of the "rim" electrode etc. Two other important characteristics of this detection system, thanks to the microbulk technology materials, are the low intrinsic radioactivity and the very low interaction probability with neutron beams. The new detector is now operational, used as a neutron beam profiler at the n_TOF facility (CERN) [25, 26], but is also considered for demanding experiments including angular distribution of products from neutron induced reactions, dark matter searches and the search of the neutrinoless double-beta decay.

5. Acknowledgements

The authors are grateful for the support of the teams from the neutron facility GELINA of JRC-Geel and from the reactor Orphée of the LLB in CEA-Saclay. We also thank the CERN's laboratory EP-DT-EF for advice and the production of the MicroMegas detectors. The initial prototype was co-funded by the Spanish project JIUZ-2013-CIE-02. This work was supported by the French Labex P2IO, by the collaboration RD51, and by the European Commission's programs EUFRAT and Eurotalents (Marie Curie Action managed by the French CEA).

[1] Y. Giomataris, P. Rebourgeard, J. P. Robert, G. Charpak, MICROMEGAS: A high granularity position sensitive gaseous detector for high particle flux environments, Nucl. Instrum. Meth. A376 (1996) 29–35.

[2] S. Andriamonje, et al., Development and performance of Microbulk Micromegas detectors, JINST 5 P02001 (2010).

[3] F. J. Iguaz, E. Ferrer-Ribas, A. Giganon, I. Giomataris, Characterization of microbulk detectors in argon- and neon-based mixtures, JINST 7 (2012) P04007.

[4] S. Cebrian, et al., Radiopurity of Micromegas readout planes, Astropart. Phys. 34 (2011) 354–359.

[5] S. Aune, et al., Low background X-ray detection with Micromegas for axion research, JINST 9 (2014) P01001.

[6] I. G. Irastorza, et al., Gaseous time projection chambers for rare event detection: Results from the T-REX project. II. Dark matter, JCAP 1601 (2016) 034. [Erratum: JCAP1605,no.05,E01(2016)].

[7] F. Belloni, F. Gunsing, T. Papaevangelou, Micromegas for neutron detection and imaging, Mod. Phys. Lett. A28 (2013) 1340023.

[8] T. Geralis, et al., A real x-y microbulk Micromegas with segmented mesh, PoS TIPP2014 (2014) 055.

[9] E. Pollacco, et al., GET: A generic electronics system for TPCs and nuclear physics instrumentation, Nucl. Instrum. Meth. A887 (2018) 81 – 93.

[10] E. Pollacco, et al., GET: A Generic Electronic System for TPCs for nuclear physics experiments, Physics Procedia 37 (2012) 1799–1804.

[11] W. Mondelaers, P. Schillebeeckx, GELINA, a Neutron Time-of-Flight Facility for High-Resolution Neutron Data Measurements, Research Infrastructures II (2006) 19 – 25.

[12] F. Aznar, et al., A Micromegas-based low-background X-ray detector coupled to a slumped-glass telescope for axion research, JCAP 1512 (2015) 008.

[13] G. F. Knoll, Radiation Detection and Measurement, John Wiley and Sons, Inc., 3rd edition, 1999.

[14] A. T. Alquezar, Development of time projection chambers with micromegas for Rare Event Searches (PhD thesis), 2013.

[15] I. G. Irastorza, et al., Gaseous time projection chambers for rare event detection: Results from the T-REX project. I. Double beta decay, JCAP 1601 (2016) 033.

[16] C. Alba-Simionesco, A. Menelle, J.-P. Visticot, The Laboratoire Léon Brillouin and the Orphée Reactor: The French National Neutron Facility, Neutron News 22 (2011) 10–13.

[17] www-llb.cea.fr/en/Web/hpr_web/HPRWEB1.php.

[18] D. McGregor, M. Hammig, Y.-H. Yang, H. Gersch, R. Klann, Design considerations for thin film coated semiconductor thermal neutron detectors-I: basics regarding alpha particle emitting neutron reactive films, Nucl. Instrum. Meth. A500 (2003) 272 – 308.

[19] P. Colas, A. Delbart, J. Derre, I. Giomataris, F. Jeanneau, I. Papadopoulos, P. Rebourgeard, V. Lepeltier, Electron drift velocity measurements at high electric fields, Nucl. Instrum. Meth. A478 (2002) 215–219.

[20] T. Böhlen, et al., The FLUKA Code: Developments and Challenges for High Energy and Medical Applications, Nucl. Data Sheets 211-214 (120) 2014.

[21] A. Ferrari, P. R. Sala, A. Fasso, J. Ranft, FLUKA: A multi-particle transport code (Program version 2005) (2005).

[22] S. Agostinelli, et al., GEANT4: A simulation toolkit, Nucl. Instrum. Meth. A506 (2003) 250–303.

[23] J. Allison, et al., Recent developments in G$_{\mathrm{EANT}}$4, Nucl. Instrum. Meth. A835 (2016) 186–225.

[24] J. Pancin, et al., Measurement of the n_TOF beam profile with a micromegas detector, Nucl. Instrum. Meth. A524 (2004) 102–114.

[25] www.cern.ch/ntof.

[26] F. Gunsing, et al., Nuclear data activities at the n_TOF facility at CERN, The European Physical Journal Plus 131 (2016) 371.

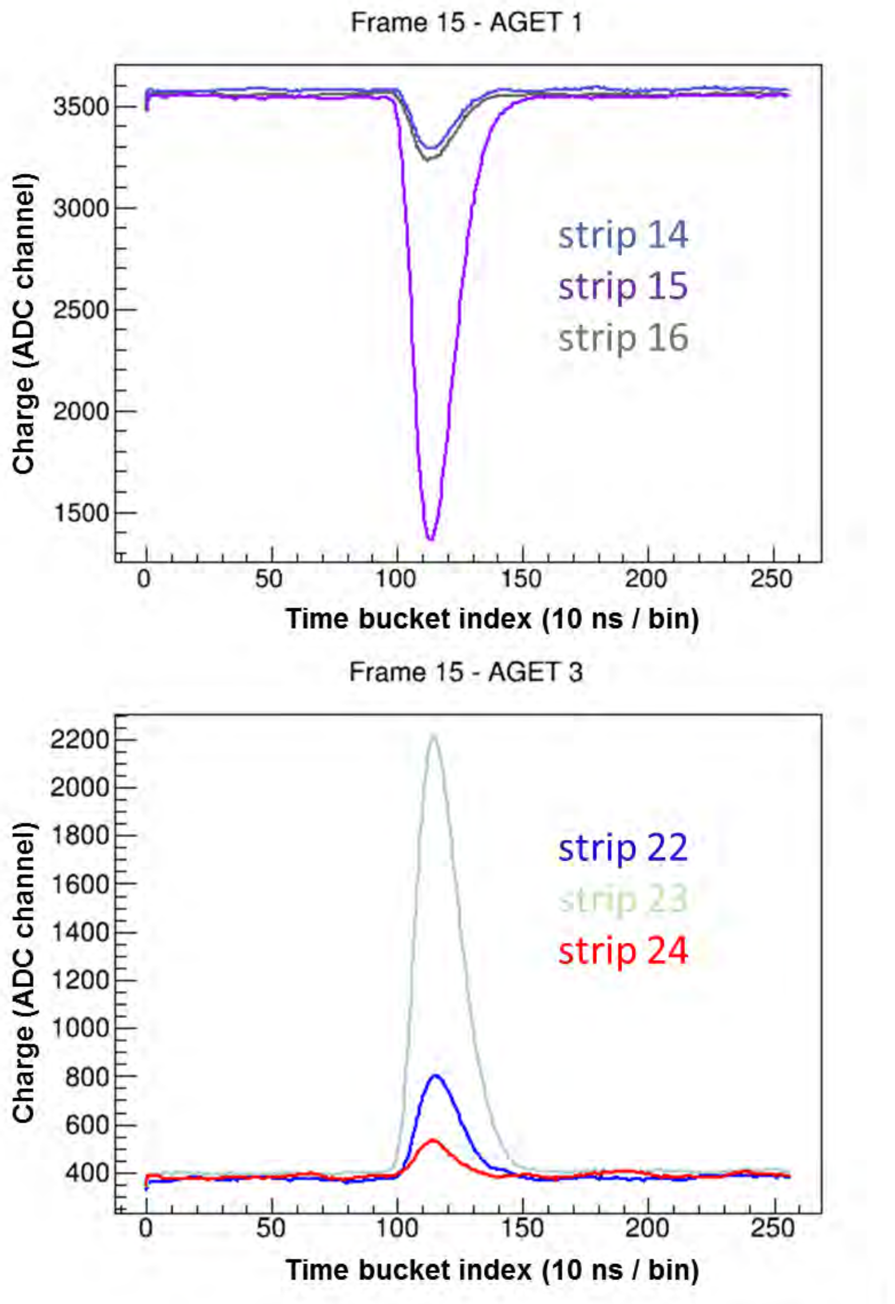

Figure 3: (Color online) Typical X-ray signal recorded from the mesh (up) and anode (down) strips, with a gas mixture of 95% Argon - 5% Isobutane (iC_4H_{10}) at atmospheric pressure. Different strip signals correspond to different colours. The full range corresponds to 240 fC charge and the sampling frequency chosen was 100 MHz.

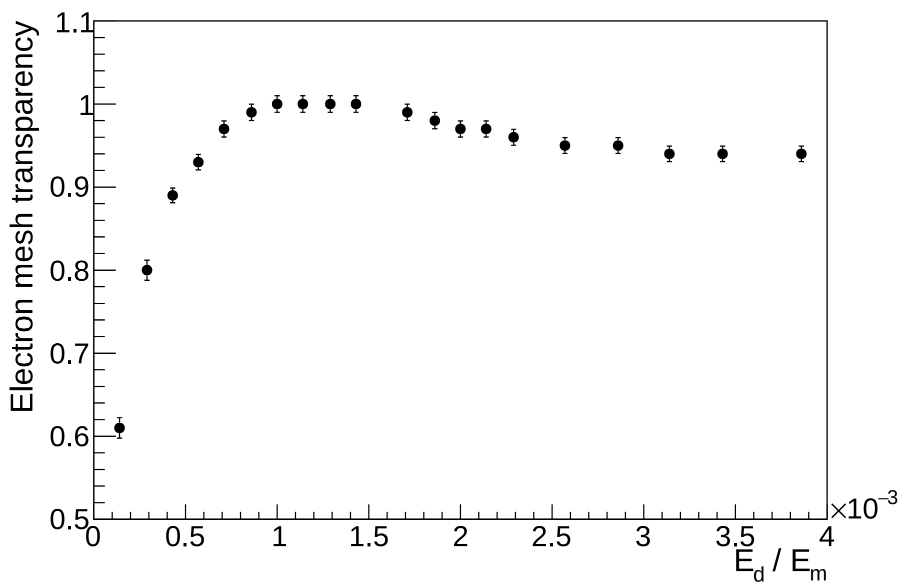

Figure 4: (Color online) Transparency curve, obtained from the position of the ^{55}Fe dominant peak in the amplitude distribution, normalised to the maximum peak position, with respect to the E_d/E_m ratio, where E_d and E_m are the electric field in the drift and the amplification region respectively.

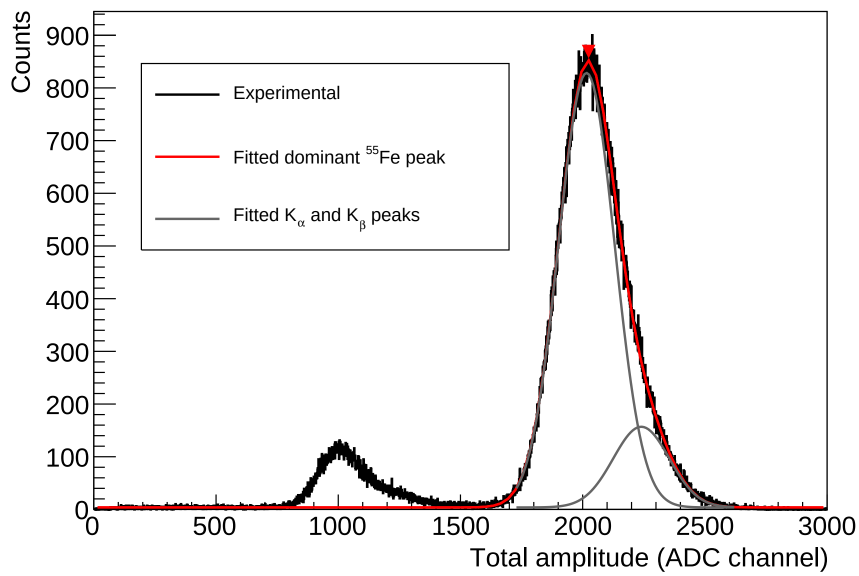

Figure 5: (Color online) Reconstructed total amplitude histogram from the anode strips from a collimated ^{55}Fe source irradiating mainly the central part of the detector (Detector No. 1). The dominant peak of the experimental spectrum (black line) was fitted with two gaussians corresponding to the K_α and K_β peaks (grey lines), the sum of which is plotted with a red line. The argon escape peak on the left is clearly separated.

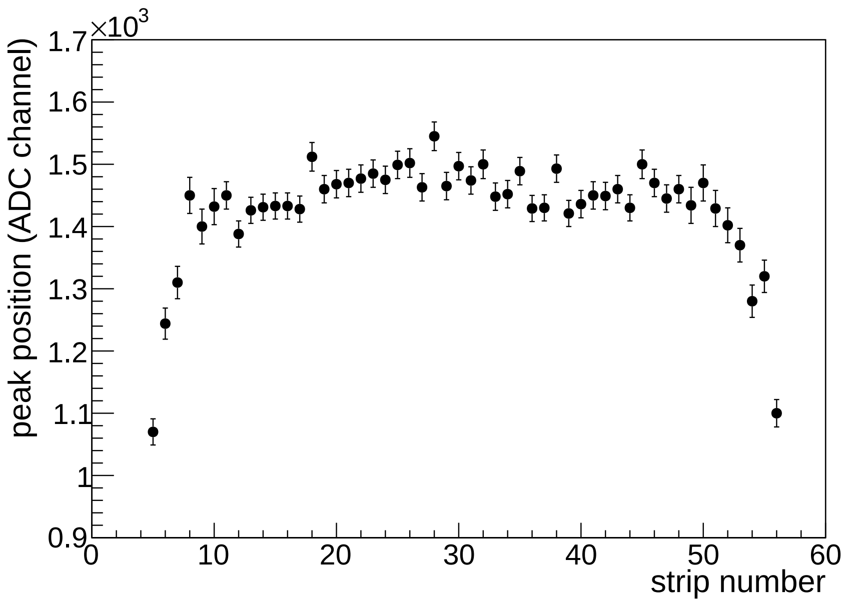

Figure 6: The dominant peak position from the energy deposition of the ^{55}Fe X-ray for the various strips (anode).

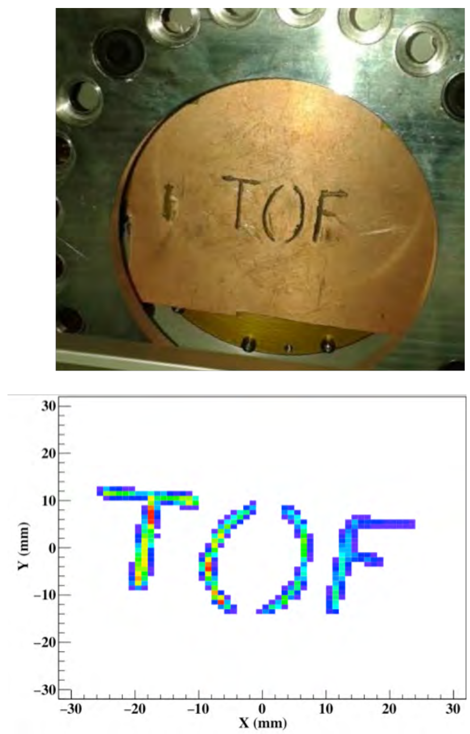

Figure 7: (Color online) Reconstruction of a copper mask using X-rays of 5.9 keV. The width of the grooves was ≈1-2 mm.

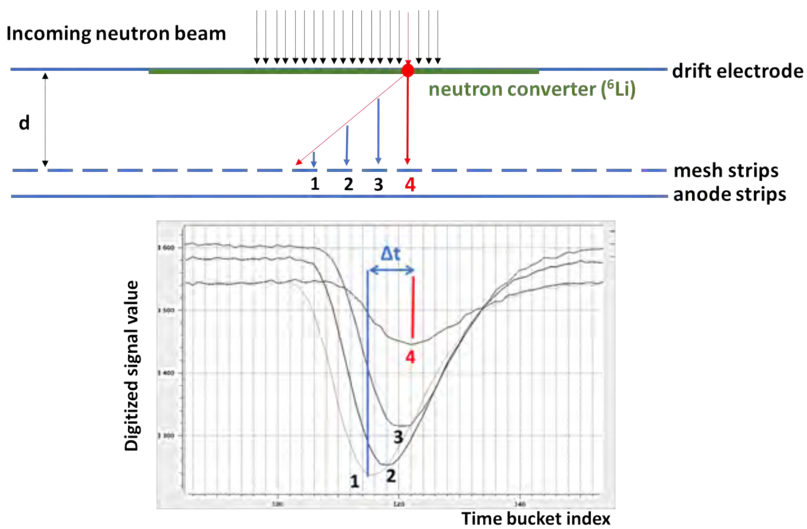

Figure 8: (Color online) Schematics of the reconstruction of the neutron beam profile. The proper neutron converter is used depending on the desired neutron energies.

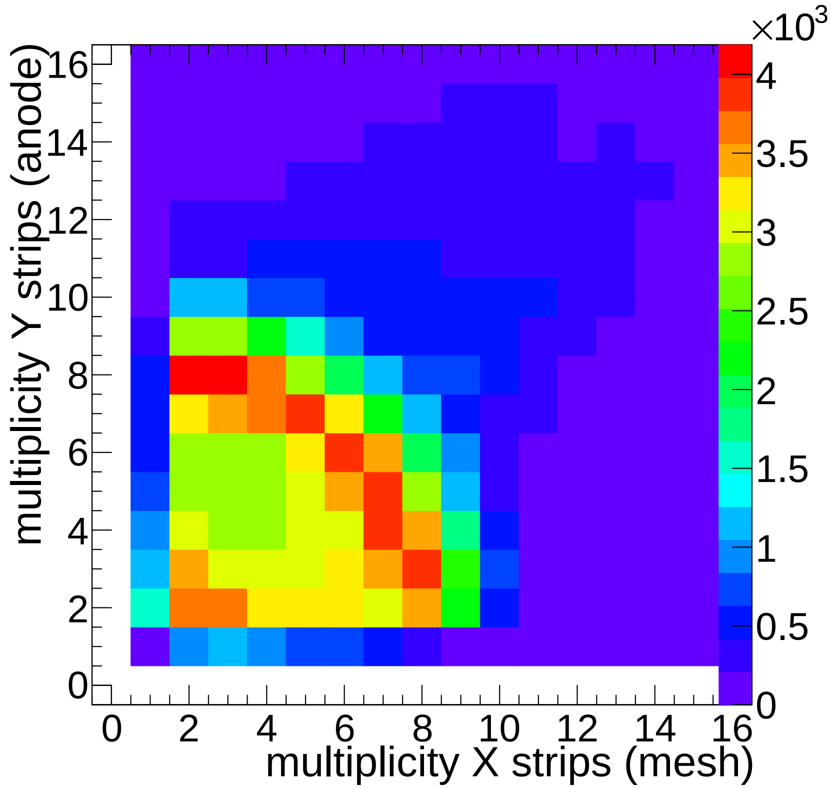

Figure 9: (Color online) Multiplicity distribution of alpha/triton tracks for the mesh and the anode strips.

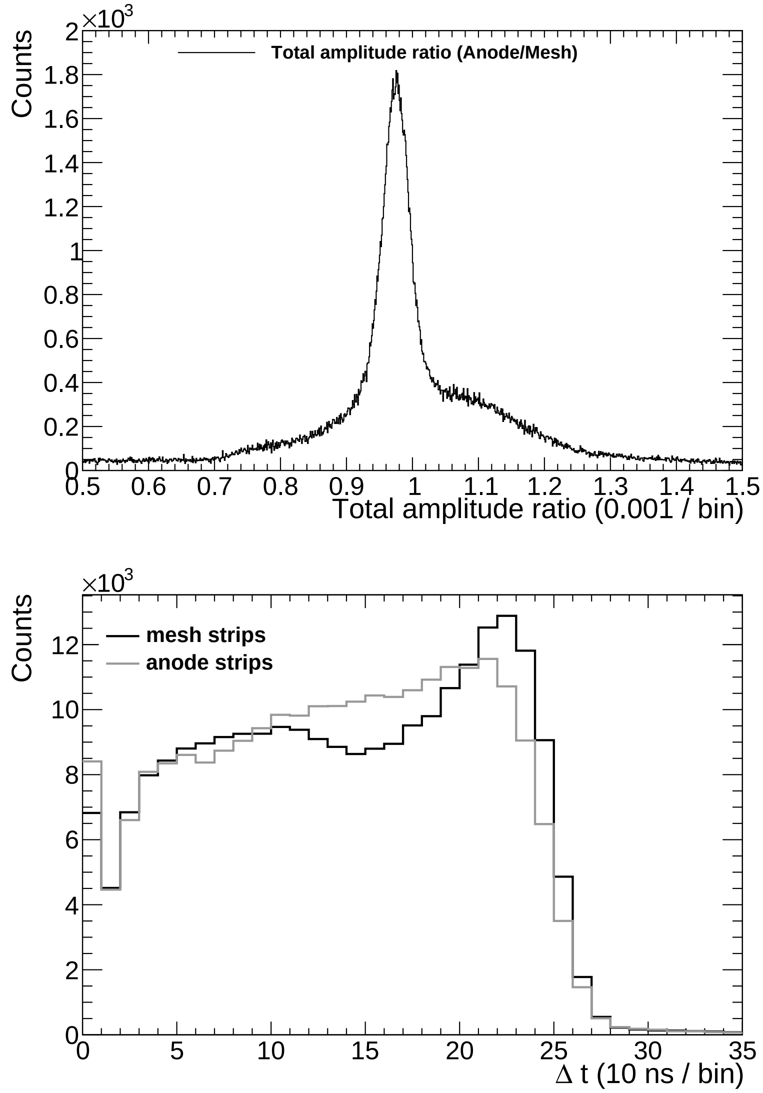

Figure 10: Up: Typical total amplitude ratio (anode strips / mesh strips) from all the alpha/triton tracks, strongly peaked at ≈1 (see text). Down: Δt distribution for the alpha/triton tracks recorded with the mesh (black) and the anode (grey) strips.

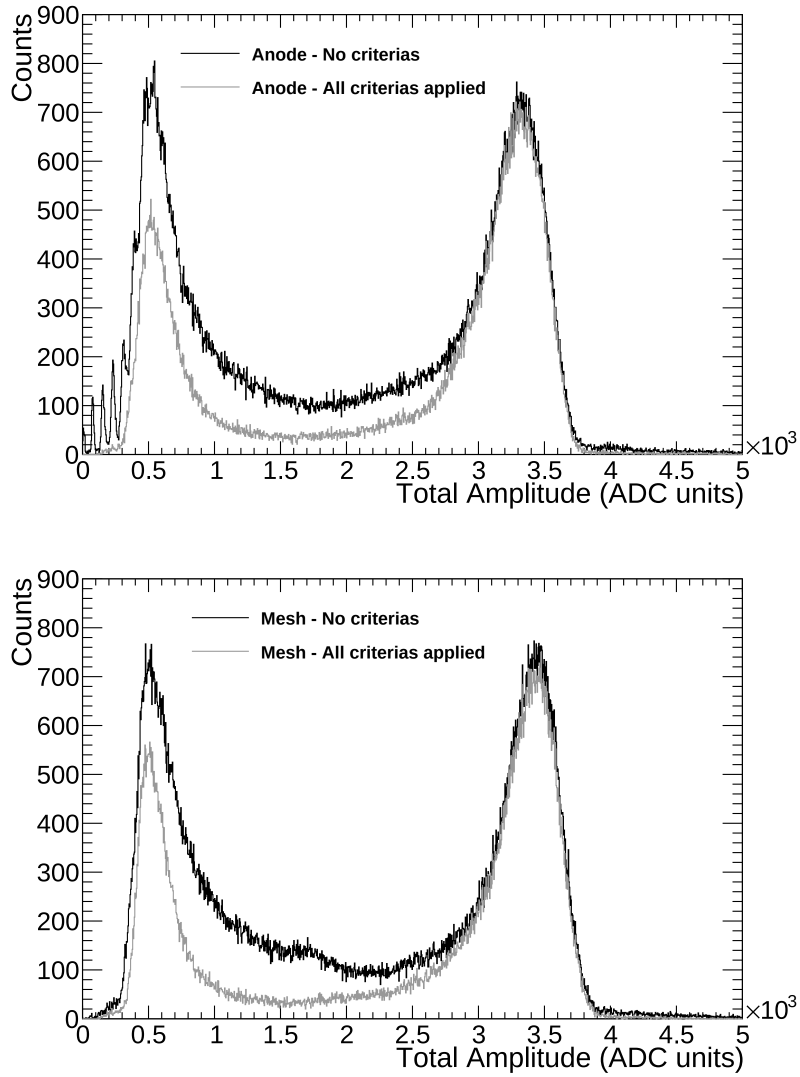

Figure 11: Reconstructed total amplitude distribution histogram, by adding the amplitudes of all the strip signals in each event, for the anode (up) and the mesh (down), from all the events (black) and only from the selected ones with the criteria applied (grey).

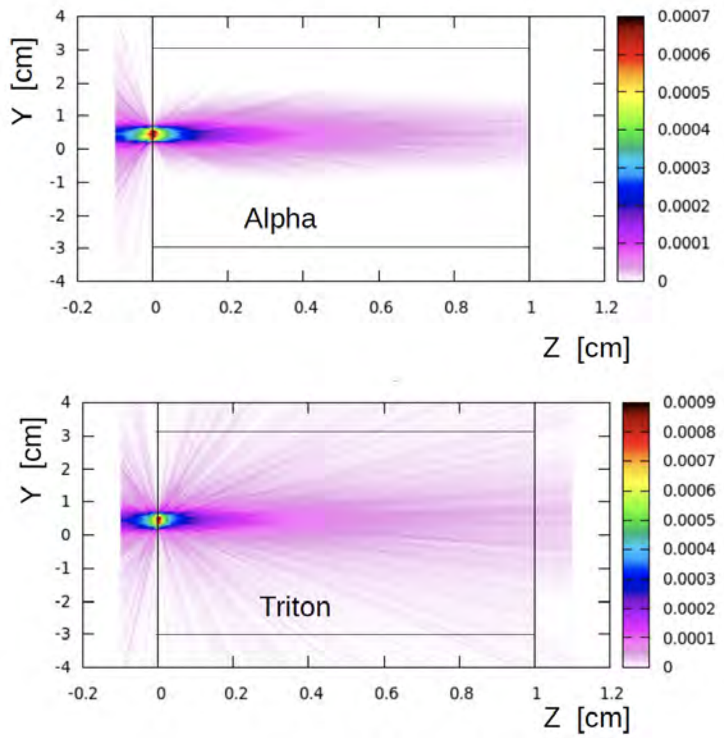

(a) (Color online) The simulated fluence (track-length density - particles/cm^2/primary) for alpha (up) and tritons (down) emitted from the ^{6}LiF layer at Z=0. The solid black lines determine the borders of the active gas volume.

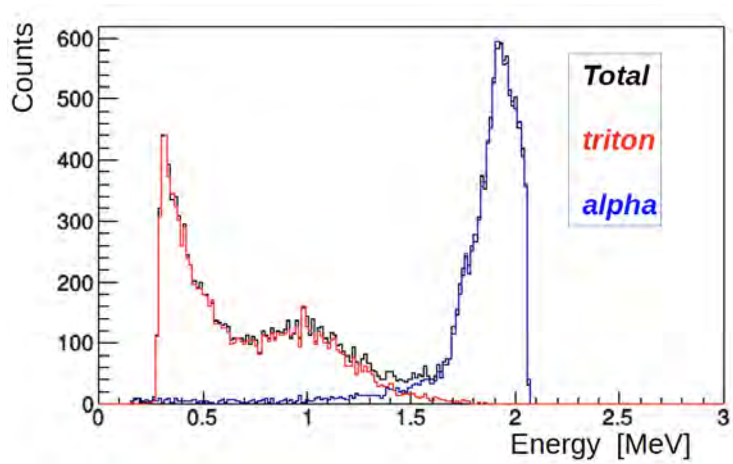

(b) (Color online) The simulated energy deposition histogram of the alphas (blue curve) and the tritons (red curve) and the sum of the two (black line) in the active gas.

Figure 12: Monte Carlo simulation results of a perpendicular thermal neutron beam of ⌀ 5 mm hitting the ^{6}LiF layer, using the code FLUKA.

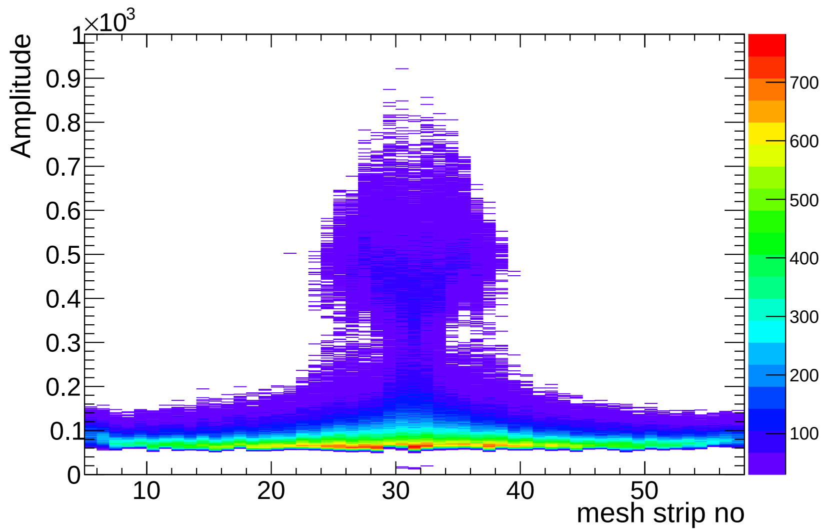

Figure 13: (Color online) Signal amplitudes as a function of the strip number (mesh strips). The neutron beam interaction point corresponds to the mesh strips 29-34. The high amplitudes at central strips correspond mainly to alpha particle tracks, while the low amplitudes recorded from all the mesh strips correspond mainly to the triton tracks, as explained in the text.

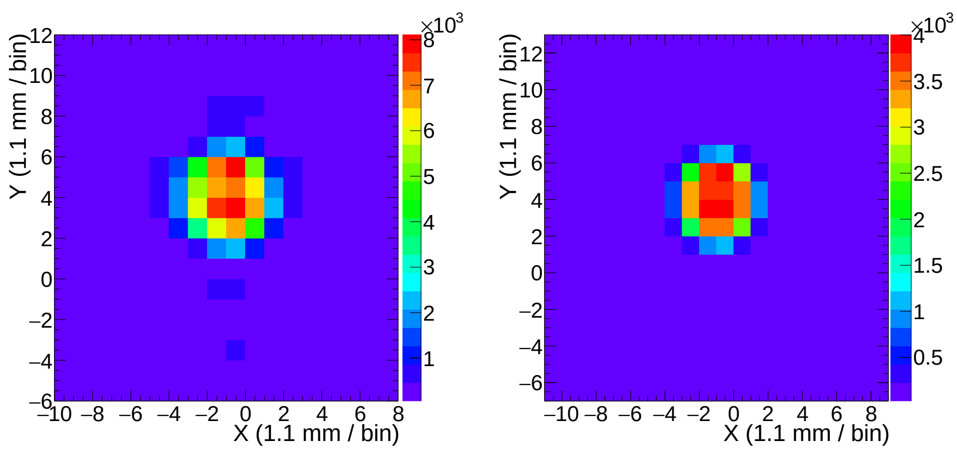

Figure 14: (Color online) Reconstructed beam profiles of the thermal neutron beam passing through the ⌀ 5 mm circular mask considering (a) all the events recorded during the acquisition (left), (b) the events chosen by applying the criteria described in the text (right).

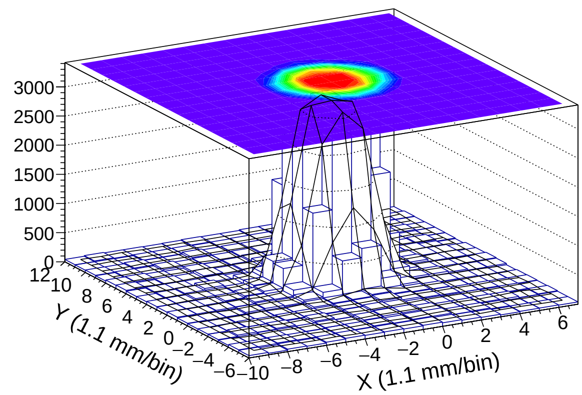

(a)

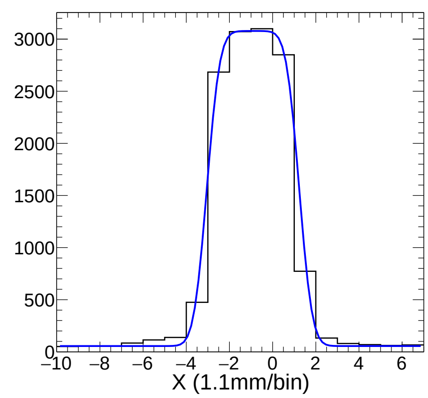

(b) 1D projection of the experimental profile (middle strip) and of the 2D function used after the fitting, for the X axis.

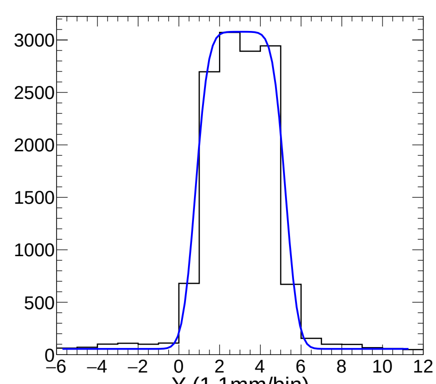

(c) 1D projection for the Y axis.

Figure 15: (Color online) An example of the 2D fitting of the experimental beam profile in order to estimate the spatial resolution of the system. The FWHM of the projections for the ⌀ 5 mm hole from the various profiles analysed was 5.0 ± 0.5 mm.

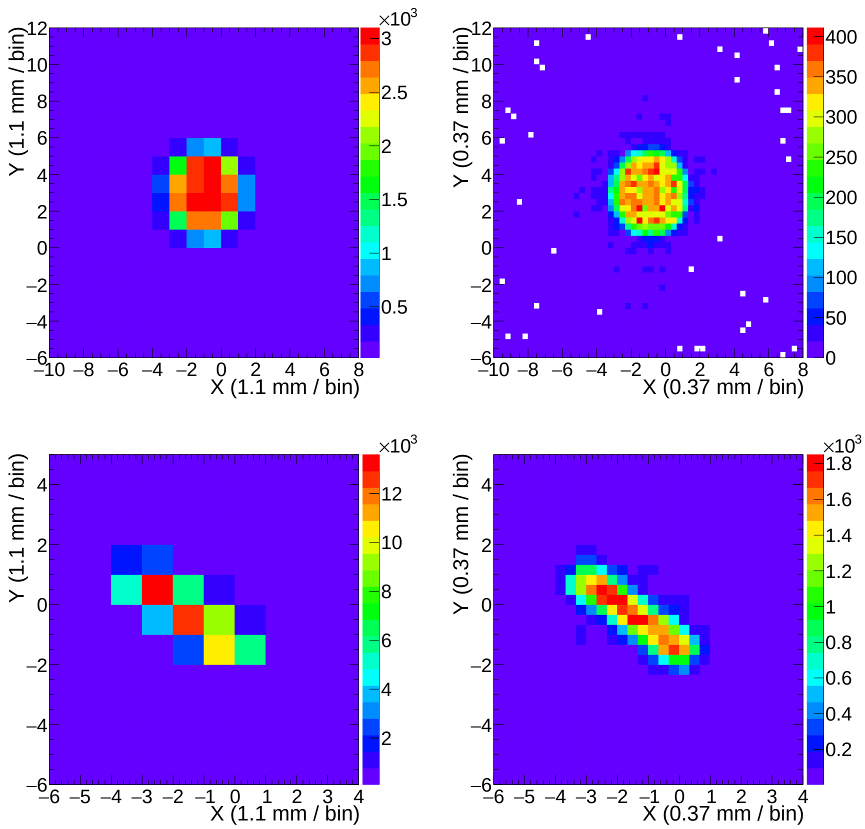

Figure 16: (Color online) Examples of reconstructed neutron beam profiles from two of the masks used. The left figures correspond to the images obtained taking the last strip into account and the right figures correspond to the refined analysis explained in the text.